

Condition Monitoring of DC-Link Capacitors Using Time–Frequency Analysis and Machine Learning Classification of Conducted EMI

Tyler McGrew¹, Student Member, IEEE, Viktoriia Sysoeva¹, Chi-Hao Cheng¹, Senior Member, IEEE, Chad Miller, James Scofield, and Mark J. Scott¹, Member, IEEE

Abstract—Condition monitoring techniques for power electronics components are important for reducing maintenance costs and increasing reliability in systems such as aircraft. This article presents a noninvasive condition monitoring system that utilizes time-frequency analysis of conducted electromagnetic interference (EMI) to classify the health of the dc-link capacitor within a three-phase inverter. The approach proposes a combined EMI filter and measurement board which is placed on the dc bus of the inverter. This board filters conducted EMI effectively and enables the inverter to comply with MIL-STD-461 G. It also enables EMI measurements to be collected for condition monitoring applications. The EMI content obtained from this board is analyzed from 15–43 MHz during switching events using a continuous wavelet transform. These characteristic switching images are used to train support vector machine models that are able to classify dc-link health into one of five health stages with accuracy up to 100%.

Index Terms—Artificial intelligence, condition monitoring, dc link capacitor, electromagnetic interference (EMI), EMI filter, prognostic and health management, support vector machine (SVM), wavelet transform.

I. INTRODUCTION

SAFE operation and maintenance are crucial elements in the transportation sector. For the airline industry, they constitute a substantial cost. Globally, more than \$14.2 billion was spent on aircraft maintenance in 2019, with an average cost of \$3.3 million per aircraft [1]. Much of this money went toward removal of equipment, however, one analysis shows that at least 40% of equipment removed is falsely diagnosed through ambiguous and labor-intensive processes [2].

As manufacturers and fleet operations continue to transition to more electric aircraft (MEA) to lower costs and reduce

greenhouse gas emissions, power electronics find increasing use in critical aircraft infrastructure. For these systems, reliable operation is paramount, and their failure may incur financial hardship and jeopardize personal safety. This concern has motivated researchers to focus on diagnostic methods for power electronics that provide real-time information about equipment status [3]–[23]. A central theme within these real-time condition monitoring systems is providing noninvasive measurements that do not interrupt the system's functionality.

There are many ways to conduct such noninvasive, online condition monitoring. Several authors use the spectral content from electrical and mechanical signals to diagnose the health of equipment [3]–[7]. In electric machines, there exists a correlation between the harmonics in the stator current and bearing damage. The authors in [3], performed spectral analysis to detect bearing health in induction machines. In [4], frequency features were extracted from motor vibrations. This data were supplied to a support vector machine (SVM) to diagnose bearing degradation, and to a support vector regression (SVR) to predict faults. Artificial neural networks (ANN) have been used to analyze changes in machine currents and voltages for fault diagnosis [5]. In [6], condition monitoring identified variations in the fifth harmonic's amplitude of inverter current to detect solder fatigue in a power module. Biswas *et al.* [7] used changes in electromagnetic radiation (EMR) signatures to diagnose the health of IGBTs and their corresponding converters in a multiconverter system.

Currently, there is much interest in condition monitoring systems for dc-link capacitors within power converters. This is due to dc-link capacitors' large size, high cost, and failure rate relative to other components [8]. Such condition monitoring systems usually aim to predict the capacitance or equivalent series resistance (ESR) of the dc-link, as these two parameters are easier to determine than others, and they provide good insight into capacitor health [9].

Most of the condition monitoring approaches for dc-link capacitors involve frequency analysis of the dc-link voltage and current. Prasanth *et al.* [10] implement a system for estimating ESR of aluminum electrolytic capacitors (AEC) in the dc-link of front-end rectifier-fed inverters. Their approach evaluated the third harmonics of dc-link voltage and current. This system requires dc-link current measurements and estimates the ESR within 4% error. Another approach, presented in [11],

Manuscript received July 7, 2021; revised October 9, 2021; accepted November 28, 2021. Date of publication January 26, 2022; date of current version June 24, 2022. This work was supported in part by U.S. Air Force under Grant FA8650-19-D-2905. Recommended for publication by Associate Editor S. K. Mishra. (Corresponding author: Mark J. Scott.)

Tyler McGrew, Viktoriia Sysoeva, Chi-Hao Cheng, and Mark J. Scott are with the Department of Electrical and Computer Engineering, Miami University, Oxford, OH 45056 USA (e-mail: mcgrewtj@miamioh.edu; sysoeva@miamioh.edu; chengc@miamioh.edu; scottmj3@miamioh.edu).

Chad Miller and James Scofield are with Air Force Research Laboratory, Wright-Patterson Air Force Base, OH 45433 USA (e-mail: chad.miller.9@us.af.mil; james.scofield.1@us.af.mil).

Color versions of one or more figures in this article are available at <https://doi.org/10.1109/TPEL.2021.3135873>.

Digital Object Identifier 10.1109/TPEL.2021.3135873

estimates dc-link capacitance and ESR in front-end rectifier-fed three-phase inverters by using the Goertzel algorithm to efficiently calculate the sixth harmonics of dc-link voltage and current. Experimental results of this approach predict capacitance within 3% error and ESR within 1% error. The work in [12] predicts ESR and capacitance using amplitude changes in the double-mains frequency as well as the switching frequency and its harmonics. The authors use a short time least square Prony's method to track the changes. The average ESR estimation is 5.66%, and the average capacitance estimation is 2.30%.

Other condition monitoring methods rely on sensors that are less invasive or already utilized in converter control loops to avoid making additional invasive measurement. In [14], an ANN predicts the dc-link's capacitance in three-phase front-end rectifier-fed motor drives. This method uses dc-link voltage harmonics with a maximum capacitance error of 1.2%. Ahmad *et al.* [15] estimate the capacitance of dc-link AEC within PV inverters. By using the second harmonic of input and output voltages and currents, they achieve a maximum error of 2.56%. In [16], a technique is presented that estimates the ESR of the dc-link AEC in a PFC boost converter using a wavelet transform-based time–frequency analysis method. This approach analyzes the output voltage of the converter in the time–frequency domain during switching events. It demonstrates the benefits of time–frequency analysis in condition-monitoring systems.

Researchers now analyze multiple variables for multiple components to determine the reliability of power electronics as a system [9]. Changes in capacitors and transistors occur at the same time, and impact the observable metrics used to diagnose the health of a single component. Machine learning approaches detect patterns that are more obscure to traditional signal processing techniques alone [4], [5], [14], [16]. The research presented here-in is a starting point to demonstrate that machine learning, in conjunction with signal processing techniques and electromagnetic interference (EMI) measurements, provides a global assessment of the components in a given system.

E-PHM is a prognostic and health management (PHM) approach that estimates the hardware's health by analyzing the spectral content found EMI [17]. EMI is highly sensitive to changes in device parameters, and this property has been used to estimate the condition of components including silicon carbide MOSFETs [18], motor bearings [19], and dc-link capacitors [20]–[23]. An attractive feature of this method is that a single source of EMI measurement provides health information for multiple components within a hardware system. This is possible since component failures have distinct spectral signatures which manifest in different areas of the frequency spectrum. Another major advantage of E-PHM is a reduction in the hardware needed to perform condition monitoring, which could make such a system more simple, versatile, and economical than other methods.

Boubin *et al.* [21] proposed a condition monitoring system for metallized polypropylene film (MPPF) capacitors in three-phase inverters using an SVM. This system works by collecting EMI data from a line-impedance stabilization network (LISN) and training the SVM to recognize changes in switching harmonic amplitudes within the EMI spectrum. The SVM uses frequency

data as features in the SVM and classify the dc-link's status into one of five health categories. A similar system is proposed in [22]. It too parses dc-link MPPF capacitors into five health classes, but its contribution is using DSP techniques along with an SVM and ANN to improve accuracy of the E-PHM system. The EMI data in [22] were collected from a current transducer (CT) placed on the dc bus, and EMI was analyzed at much higher frequencies (10s of MHz). Additionally, the approach in [22] employs a hidden Markov model (HMM) to improve its classification results, achieving a 94.9% average classification accuracy. The research presented in [23] builds on the work of [21] and [22], by creating a similar MPPF dc-link health classification system using CT data with machine learning classification and HMM correction. However, this system analyzes the collected EMI data in the time–frequency domain using a continuous wavelet transform (CWT) and a convolutional neural network (CNN) for image classification. This approach achieved 99.9% classification accuracy using both two-layer and four-layer CNNs.

The condition monitoring method proposed in this article builds off of several techniques presented in [21]–[23]. It is important to compare this research with respect to other available methods. Most condition monitoring approaches attempt to extract precise measurements of ESR and dc-link capacitance to predict the capacitor health [9]. This article, on the other hand, separates capacitor health into five distinct classes based that are based on the training data obtained at specific ESR and dc-link capacitance values.

This research demonstrates that a broad understanding of component health is available from EMI measurements, using signal processing techniques and support vector machines (SVM). To achieve this, it uses time–frequency analysis of conducted EMI measurements, along with an SVM model, to classify the health of the MPPF dc-link into one of five classes. Another contribution of this article is incorporating sensing elements into an EMI filter to obtain the spectral data. This hardware filters conducted EMI on the dc bus, while also providing measurements of common-mode (CM) and differential-mode (DM) EMI for condition monitoring analysis. The EMI measurements collected from this board are converted into time–frequency images using a CWT, and switching events are identified and averaged to create characteristic switching events of EMI spectral content versus time around 15–43 MHz. Finally, these characteristic switching events are used to train and evaluate an SVM which makes dc-link health classifications between one of five health categories. The accuracy of this method approaches 100%.

The rest of this article is organized as follows. Section II describes the design and function of the proposed EMI filter and measurement board. Section III provides background on the ageing process of film capacitors before explaining the electrical mechanism which serves as the basis for the condition monitoring system. Section IV gives an overview of the theory and implementation for each step in the dc-link classification system. Section V details the process of data collection and provides experimental results. Finally, Section VI concludes this article.

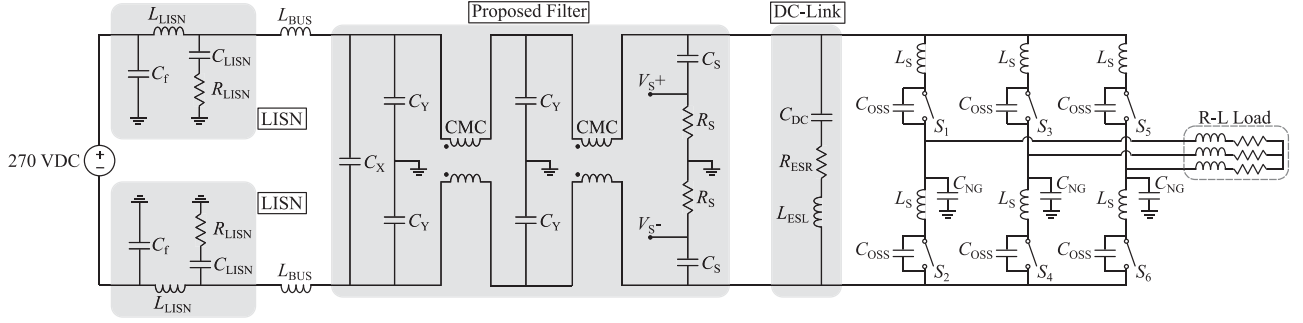


Fig. 1. Lumped-element model of the proposed EMI filter and measurement board attached to three-phase inverter with dc-link, R - L load, and LISNs.

TABLE I
SUMMARY OF KEY ELECTRIC COMPONENTS WITHIN THE PROPOSED EMI FILTER AND MEASUREMENT BOARD

Part Ref.	Description	Manufacturer	Part Number	Quantity	Value
C_S	Sense capacitor	WIMA	FKP2O101501D00JSSD	2 x 5	150 pF
R_S	Sense resistor	Bourns Inc.	CR2512-JW-103ELF	2 x 5	10 k Ω
CMC	Choke	Pulse Electronics Power	PH9455.705NL	2	6.5 mH @ 1.52 MHz
C_Y	Y-capacitor	KEMET	R413N315050T1K	4	150 nF
C_X	X-capacitor	KEMET	R46KI3100JPM1K	1	100 nF

II. EMI FILTER AND MEASUREMENT BOARD

A lumped-element model of the proposed condition monitoring system is shown in Fig. 1. This model includes the 270 Vdc power supply, two LISNs, the proposed EMI filtering and measurement board, the MPPF dc-link capacitor, and a three-phase inverter with R - L load. For high-frequency EMI analysis, the switching devices are modeled as ideal switches (S_i) with output capacitance (C_{OSS}) and series inductance (L_S). Additional parasitic capacitances exist between the inverter's output and ground (C_{NG}) due to the capacitance between the heatsink and the devices' dies. Stray inductances also occur between the LISNs and the terminals of the proposed filter (L_{BUS}).

Images of the front and back of the proposed EMI filter and measurement board are shown in Fig. 2. The board consists of a high-pass EMI measurement section with BNC connectors from V_S+ and V_S- to ground, followed by two filtering stages consisting of CM chokes (CMC), line-to-ground capacitors (Y-capacitors), and one line-to-line capacitor (X-capacitor). Additionally, there are terminals on both the HVdc input and inverter output sides for electrical connections. Within the proposed condition monitoring system, this board would replace the traditional EMI filter and stay permanently attached to the inverter. Since the use of this EMI filter/measurement board does not require design changes or affect the operation of the inverter itself, the proposed condition monitoring system is noninvasive and could be used during normal (online) converter operation.

The EMI filtering performance of the board should be demonstrated to meet application-standard emission levels in order to prove efficacy of its filtering performance. Therefore, the board's filter is designed to meet conducted EMI standards laid out in the United States Department of Defense Interface Standard MIL-STD-461G [24]. Specifically, the EMI filtering performance is tested in Section V-A according to standard

CE102 for conducted emissions from 10 kHz to 10 MHz on the HVdc power lines.

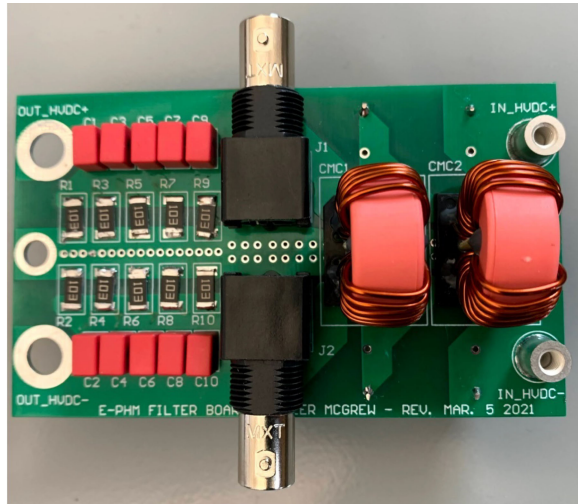
A summary of key components in the board can be found in Table I. Simulation results and experimental data from a previous iteration of a filter/measurement board design demonstrated that a single filter stage consisting of CMC and Y-capacitors was not sufficient to filter EMI harmonic content across the entire frequency range due to excessive CM noise. Therefore, a two-stage filter was designed with the aim of reducing CM noise using two sets of CMCs and Y-capacitors.

First, CMCs were selected with the highest possible CM inductance and resonant frequency. Large CM inductance is important to provide a low-corner frequency, while minimizing the required Y-capacitance, which reduces ground leakage current. For this design, a CMC was selected with 6.5 mH of CM inductance at 1.52 MHz, manufactured by Pulse Electronics Power. Then, Y-capacitance was chosen to be a moderate value of 150 nF. The corner frequency for CM voltage attenuation of the filter is

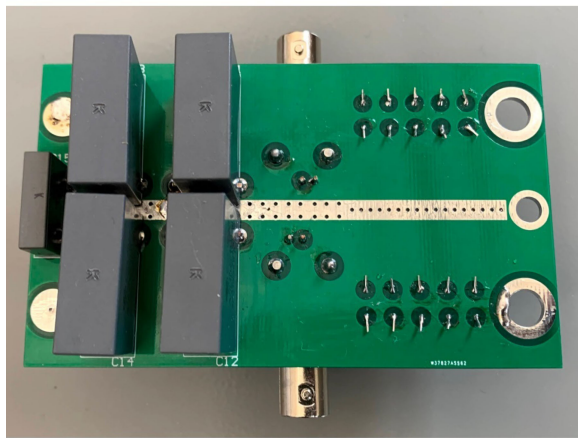
$$f_{c,CM} = \frac{1}{2\pi\sqrt{L_{CMC}C_Y}} = 5.1 \text{ kHz} \quad (1)$$

and has a magnitude roll off of 80 dB per decade. Therefore, there is ideally 160 dB of CM attenuation at 500 kHz, not including any filtering provided by the sensing branch of the filter/measurement board.

For this application, DM noise is less of an issue than CM noise, so just one X-capacitor was placed on the dc input side of the filter with a value of 100 nF. Additional DM filtering is provided by leakage inductance of the CMCs, the Y-capacitors, and the dc-link capacitor itself. Not including the dc-link's DM filtering, the DM voltage attenuation of the EMI filter should be 80 dB per decade. However, the poles of the filter's gain plot will



(a)



(b)

Fig. 2. (a) Top and (b) bottom of EMI filter and measurement board.

be at higher frequencies than $f_{c,CM}$ due to the smaller values of the DM filter components.

The EMI sensing section of the board consists of two RC high-pass filters with BNC connectors referenced to ground. This branch is intended to act similarly to the measurement portion of an LISN. Therefore, for demonstration purposes, the sensing branch of this board is designed to be used with $50\text{-}\Omega$ measurement impedances at the BNC connectors from V_S+ and V_S- to ground. In case the measurement impedances are not attached, R_S resistors are required to provide current return paths and discharging for C_S capacitors. For this design, R_S was chosen to be $2\text{ k}\Omega$, similar to typical values seen in LISNs for this component.

Then, the value of C_S needs to be high enough to provide a small impedance at frequencies of interest. In other words, the cutoff frequency ($f_{c,S}$) of the high-pass RC filters at sensing points V_S+ and V_S- needs to be below the EMI frequencies of interest. As explained in Section III, the EMI spectral content of interest in this application is between $15\text{--}50\text{ MHz}$. Therefore,

C_S was chosen to be 750 pF , such that

$$f_{c,S} = \frac{1}{2\pi(R_S \parallel 50\text{ }\Omega)C_S} = 4.35\text{ MHz} \quad (2)$$

which is below the lower end of the given frequency range.

As mentioned previously, the $50\text{-}\Omega$ measurement impedance used for this board design was chosen to reflect the typical EMI measurement process using an LISN with $50\text{-}\Omega$ probe and measurement equipment impedances. In this design, to ensure safe power dissipation within the sensing branch components, R_S and C_S were paralleled in sets of five. However, in a practical application of the proposed condition monitoring system, it would be advantageous to use a high measurement impedance, such as an ADC measuring across $R_S = 100\text{ k}\Omega$. Using a higher measurement impedance reduces component power dissipation, size, and cost. In addition, a larger measurement impedance increases the measurement bandwidth into lower frequencies by decreasing $f_{c,S}$, which might be useful in a different application of this type of condition monitoring system.

MPPF capacitors were used for the X-capacitor, Y-capacitors, and sensing capacitors. These film capacitors were chosen due to their ability to maintain their capacitance with a large (270 V) dc bias. This dc capacitance stability is in contrast to multi-layer ceramic capacitors (MLCCs), which have similarly good high-frequency filtering performance, but suffer from a large drop in effective capacitance when a dc bias voltage is present. Additionally, film capacitors are well suited for EMI filtering due to high surge voltage and ripple-current ratings.

Once components were selected, the board layout of the filter PCB was designed to maximize effective EMI filtering and minimize the addition of any detrimental parasitic effects. Wide polygon pours were used in lieu of traces, and many ground vias were added along the length of the board to minimize ground impedance. Additionally, BNC connectors were placed as close as possible to the RC EMI sensing legs to minimize measurement impedance.

III. CONDUCTED EMI MECHANISM OF INTEREST

Film capacitors are finding increasing use in dc-link applications due to favorable characteristics, such as high dielectric voltage strength, low dissipation factor, and good capacitance stability [8], [25]. They can be modeled by a simplified equivalent circuit consisting of a capacitance (C_{DC}), series resistance (R_{ESR}), and series inductance (L_{ESR}) [26].

Metallized film capacitors, such as MPPF capacitors, have the ability to self-heal when local breakdowns occur in their dielectric [25]. When a region of the dielectric experiences a breakdown event due to a localized short, the electric discharge causes the electrode layer to heat up and evaporate. This self-healing property isolates the defective portion of the capacitor and prevents a short-circuit failure of the capacitor.

The same self-healing property of MPPF capacitors also serves as a primary mechanism for their ageing [26]. As local breakdowns occur and sections of the capacitor's electrodes evaporate, the reduced surface area causes a decrease in effective C_{DC} . Excessive evaporation within the capacitor also leads to

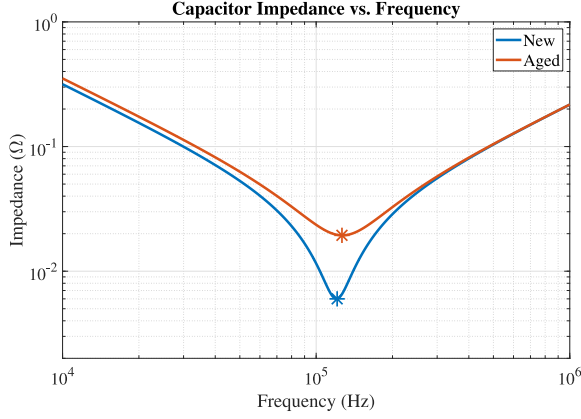


Fig. 3. Capacitor impedance versus frequency for new and aged MPPF capacitors.

corrosion on the metallized layers, which increases R_{ESR} . The L_{ESL} of the capacitor remains fixed over time, however, as the inductance is only dependent on the geometry of the capacitor [8].

The change in impedance of an MPPF capacitor over time due to ageing is demonstrated in Fig. 3. The parameters of the new capacitor are: $C_{DC} = 50 \mu\text{F}$, $R_{ESR} = 6 \text{ m}\Omega$, and $L_{ESL} = 35 \text{ nH}$, and the aged capacitor parameters are: $C_{DC} = 45 \mu\text{F}$, $R_{ESR} = 19.4 \text{ m}\Omega$, and $L_{ESL} = 35 \text{ nH}$. As the capacitor ages, its resonant frequency (f_{res}) increases due to a decreased C_{DC} in conjunction with a fixed L_{ESL} . At the same time, the impedance of the capacitor increases at f_{res} , where the series impedances of C_{DC} and L_{ESL} cancel out, due to the increase in R_{ESR} .

These changes in impedance affect the capacitor's ability to minimize voltage ripple on the dc bus. The condition monitoring system proposed in this article analyzes changes in spectral content of conducted EMI from 15–43 MHz to predict dc-link health. The primary cause of conducted EMI within this frequency range is a ringing of parasitic capacitances and inductances within the commutation loop of the inverter during switching events. Time–frequency analysis of DM noise in this frequency range is used to compare changes in frequency, amplitude, and duration of ringing during inverter switching events.

A modified version of the circuit model from Fig. 1 is shown in Fig. 4. This lumped parameter is based on a high-frequency analysis of the conducted DM EMI within the inverter and filter system during a switching event. In this model, the dc-voltage source, LISNs, and L_{BUS} are removed since conducted EMI generated by the inverter is greatly attenuated by the EMI filter before reaching these components. Series inductances ($L_{L,X}$, $L_{S,Y}$, and $L_{S,S}$) are included with the capacitors in the filter due to the significant inductive impedance in these components within the frequency region of interest. Similarly, C_{DC} is replaced by a stiff voltage source (v'_{dc}) equal to the voltage across the dc-link due to its large capacitance relative to the high frequencies of interest. The load is dominated by L_{LOAD} above switching frequency and is therefore replaced with a current source, which appears as an open circuit when superposition is applied. Since

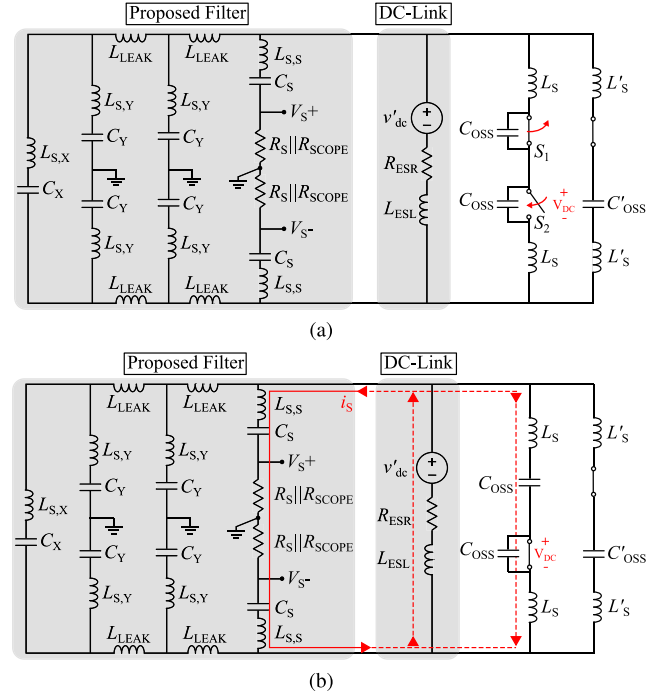


Fig. 4. Circuit model from Fig. 1 modified for high-frequency DM EMI analysis (a) before and (b) after S_2 closes and S_1 opens (S_3 and S_5 are closed for both states).

the model is for DM analysis, CMCs are replaced with DM leakage inductances, and neutral-to-ground capacitances (C_{NG}) are removed from switching branches in the inverter.

In Fig. 4(a), S_1 , S_3 , and S_5 are assumed to have been on long enough so there is no ringing in their branches. The branches of S_3 and S_5 are modeled in parallel so that $L'_S = \frac{1}{2} L_S$, $C'_{OSS} = 2C_{OSS}$, and $C'_S = 2C_S$, assuming equal parasitic values for both branches. The C_{OSS} of S_2 is charged to V_{DC} .

At this point, S_1 is turned OFF and S_2 is turned ON simultaneously in a hard-switching event. Fig. 4(b) shows the model from Fig. 4(a) just after this switching event occurs. While the C_{OSS} of S_1 is charging and the C_{OSS} of S_2 is discharging, an underdamped oscillating circuit is formed between the sensing leg of the filter, the dc-link capacitor, and the three legs of the inverter. In particular, a resonant DM circuit is formed between the dc-link and the parasitics (L_S , C_{OSS}) in the switching leg containing S_1 and S_2 . The approximate values of these parasitic components are known, and the resulting resonant frequency of this commutation loop should be about

$$f_{res} \approx \frac{1}{2\pi \sqrt{(L_{ESL} + 2 * L_S)(C_{OSS})}} = \frac{1}{2\pi \sqrt{(12 \text{ nH} + 2 * 20 \text{ nH})(1 \text{ nF})}} = 22.1 \text{ MHz}. \quad (3)$$

The time–frequency profile of this loop's DM ringing changes as the MPPF dc-link capacitor ages. As R_{ESR} increases, the increased damping should cause a reduction in both the amplitude and duration of ringing. Since the series capacitance of this loop

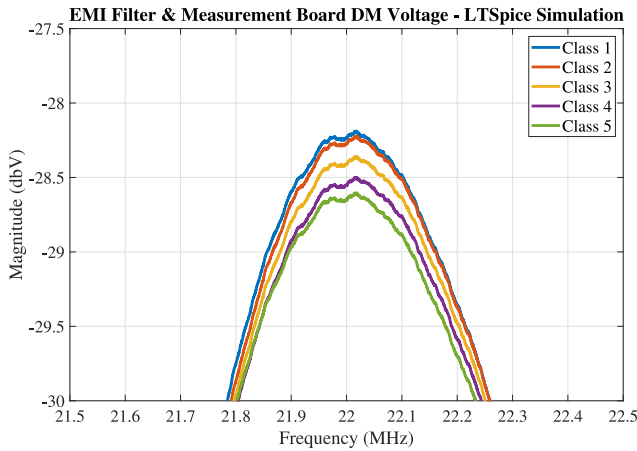


Fig. 5. SPICE simulation results for DM EMI measurements from proposed EMI filter and measurement board, smoothed with low-pass filter.

is dominated by C_{OSS} , the decrease in dc-link capacitance should not cause a significant change in resonant frequency.

This resonant noise around 22 MHz passes through the sensing branch of the filter/measurement board. Simulation in SPICE supports this conclusion, as shown in Fig. 5. So, time–frequency analysis of the EMI data collected from the proposed filter board should prove effective in determining changes in dc-link series resistance, and therefore dc-link capacitor health.

Recent research [27] explores health measurements for individual capacitors in a dc-link. The procedure requires individual capacitor measurements prior to creating the dc-link and installing it into a PV inverter. Then, the temperature of each capacitor is estimated based on these characteristics, and it is used in a physics-of-failure model to predict the individual health of each capacitor in the dc-link using a Kalman filter. This research, on the other-hand, treats the dc-link as single, homogeneous unit, and it assumes all capacitors in the dc-link age at the rate same. While it may be possible to apply techniques like [27], or others, this is outside of the scope the present study and can be clarified in future research.

It is important to fully understand the scope and limitations of the proposed condition monitoring mechanism, which is based on changes in DM EMI damping due to ageing of the dc-link. In particular, the proposed condition monitoring method analyzes changes in the damping of the resonant loop shown in Fig. 4(b). As the dc-link ages, this overall loop resistance will increase; however, the dc-link does not constitute the only series resistance within this loop. The power devices within the switching legs of the inverter have their own $R_{DS(on)}$ which contribute to the overall loop resistance. There are other factors that may impact condition monitoring performance by affecting the loop resistance, such as the use of shunt resistors within the dc-link.

To understand potential limitations of the proposed system, it is also important to foresee how the impedance of other components within the inverter will change over time, and how these changes may affect condition monitoring performance. Since this system is only concerned with EMI content around

22 MHz, the EMI filter portion of the system in Fig. 4(b) can be considered an open circuit and ruled out from affecting the condition monitoring system. Inductances within the system are based on geometries which should remain constant during inverter operation. The impedance of the sensing leg is high due to large R_S , so ageing of C_S should not affect the resonant EMI mechanism of interest, nor change $f_{c,s}$ to affect EMI sensing. Therefore, it seems the only impedances which may change over time and significantly affect the condition monitoring system are the total commutation loop series capacitance and resistance. Notably, this includes the C_{DC} and R_{ESR} of the dc-link capacitor, and the C_{OSS} and $R_{DS(on)}$ of the power devices.

Not all operational conditions or possible adverse effects have been tested as part of this research. However, the proposed condition monitoring system should be viable for any three-phase inverter so long as the change in the dc-link's R_{ESR} due to ageing is the primary mechanism affecting a change in overall commutation loop resistance during the lifetime of the dc-link capacitor. This is a broad qualifying statement and future research is needed to determine the specific efficacy of the proposed condition monitoring system under different operating conditions, temperatures, switching devices, etc.

It is worth noting that the test setup for this research uses transistors with an $R_{DS(on)}$ of 120 m Ω (Rohm SCT2160KE), which is at least 40-times bigger than the ESR of the capacitors (1 to 3.3 m Ω). Even though the ESR of the dc-link is much smaller than the devices' ON-resistance, the proposed algorithm operates based off of changes in commutation loop damping. Throughout this testing, transistors were operated under very similar conditions. The power level remained constant and there was minimal variation in the power device's temperature.

CM EMI measurements offer another degree of freedom to address the effect of simultaneous switching device ageing on dc-link health condition monitoring. CM noise is strongly influenced by the power devices' characteristics with less impact from the dc-link capacitor. DM noise, on the other hand, strongly depends on the dc-link capacitor with reduced impact from the power device. The EMI filter/measurement board proposed in this article enables both CM and DM measurements for condition monitoring use. Therefore, future research could take advantage of these two degrees of freedom to simultaneously monitor health of dc-link and power devices, while improving the accuracy of each. This would be a potential application for the short time least square Prony's method mentioned in [12].

IV. CAPACITOR CLASSIFICATION SYSTEM

The classification system for predicting dc-link capacitor health uses a SVM to predict dc-link health between one of five discrete health classes based on time-frequency images of conducted EMI during inverter switching events. A continuous capacitor health (regression-based) approach was also considered. However, classifying the dc-link into one of five health stages has clear practical meaning for an operator and is generalizable between different applications, compared with a continuous-valued ESR prediction. This is not to say that a continuous regression approach is inferior, and either approach

should produce a similar end result. For this research, the five capacitor health stages are defined in Section V and each represents a distinct phase of the capacitor's life cycle to give a clear meaning of component health, ranging from new to aged.

In this section the classification process is explained as follows: First, DM time-domain EMI data collected from the EMI filter is processed into time-domain images using a CWT. Then, switching events within these images are located, isolated, and averaged together to form representative switching events in the time-frequency domain. Finally, each of these images are flattened into a 1-D feature vector. Many feature vectors from each of the five capacitor health classes are used to train the SVM, while only one feature vector that is needed for condition monitoring is used (SVM classification) thereafter.

A. Continuous Wavelet Transform

The first step in the classification system is to split time-domain EMI data into subsamples, which can be converted into time-frequency domain images. The length of each subsample is defined as testLength and is chosen to be equal to the switching period of the inverter, where $T_s = 50 \mu\text{s}$. The sampling rate is 100 MSample/s, so

$$\text{testLength} = 50 \mu\text{s} * 100 \text{ MSample/s} = 5000.$$

Since each subsample contains time domain EMI amplitudes for one full T_s , each corresponding time-frequency domain image will contain EMI data for the six switching events within the three-phase inverter during this period. This is visible in step 1 of Fig. 6, where each switching event corresponds to a spike in the DM voltage. The magnitudes are different because the magnitudes of the current in each phase are not the same. At this point, the EMI data are ready to be converted into images.

There are several methods for transforming 1-D time domain data into 2-D time-frequency data. A basic method of such time-frequency analysis is the short-time Fourier transform (STFT), where a window function of fixed length is moved along the 1-D signal and the Fourier transform is computed at each section.

Another method of time-frequency analysis, the CWT, improves upon the STFT by analyzing the 1-D signal at different resolutions for different frequencies. This adaptive resolution property of the wavelet transform improves the time-resolution of high-frequency bins compared with the STFT. The time resolution of high-frequency signal components is critical for this application, because the time-frequency images need to accurately capture the duration of high-frequency ringing from the time-domain data. For this reason, a CWT is used in this system.

However, Fourier-transform based time-frequency techniques rely on infinite-length sine and cosine functions as a transform basis, CWTs rely on wavelet basis functions. The specific wavelet function used for an application can vary, but the key property of wavelet functions is time localization, in addition to frequency localization. All commonly used wavelets can be described by a generalized, analytic Morse wavelet function, as shown in [28]. For this research, an analytic Morse wavelet was chosen, with symmetry parameter equal to 3, time-bandwidth

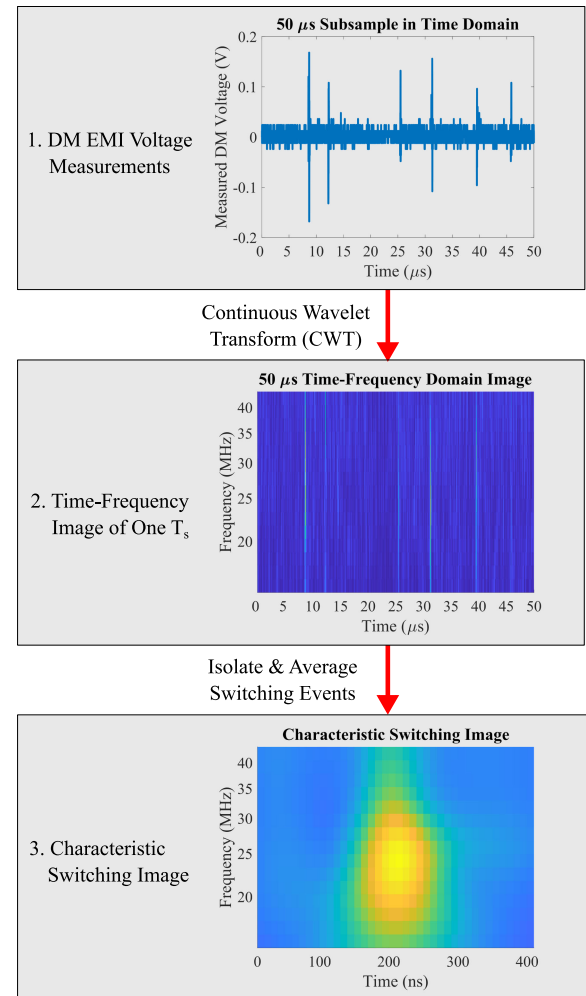


Fig. 6. Overview of the dc-link health classification system showing the steps for transforming and processing conducted EMI data for SVM classification.

product equal to 60, and 10 voices per octave. This transform was found empirically to produce good results in terms of time and frequency resolution.

At this point in the classification process, each subsample of data is transformed into a real-valued time-frequency image using the CWT, as shown in step 2 of Fig. 6. Each image is cropped along the vertical axis to only contain frequency content from 15 to 43 MHz. The minimum frequency limit, 15 MHz, is chosen to limit image size and remove unnecessary frequency content. The maximum frequency limit, 43 MHz, is the upper frequency limit available using the CWT with the 100 MSample/s time-domain data.

Once the time-frequency images are created for each T_s , the next step is to locate each of the six switching events, as they contain the EMI content of interest. First, the maximum amplitude along the (vertical) frequency domain is taken at each point in time on the image to create a (horizontal) time domain vector of peak amplitudes. Then, a peaks detection algorithm is used to find the locations and prominences of local maxima within the time domain vector, with a minimum peak-to-peak distance of 70 ns. Finally, the locations (time positions) of the

six switching events are defined by the locations of the six peaks with the largest prominence.

Once the locations of the switching events within the time-frequency image are known, the next step is to isolate and average multiple switching events to create an input feature vector for the dc-link classification algorithm. First, six switching event images are created by taking the time-frequency image from step 2 and cropping the image along the time (horizontal) axis at the locations of the six switching events. Each of these switching event images have a fixed width of 410 ns, centered on the peak amplitude of the switching events, to succinctly display the full profiles of high-frequency EMI ringing. If one of the switching events is less than 210 ns from the edge of the image, it is simply skipped over. Then, these switching event images are averaged to reduce noise and improve training and classification outcomes.

This process is then repeated for a number of time-frequency images so that a number of averaged switching events exist, each corresponding to one T_S of EMI data. To further decrease noise and improve classification results, these averaged switching images are themselves averaged to create a characteristic switching image of up to 50 T_S and 300 averaged switching events. An example characteristic switching image is shown in step 3 of Fig. 6. Finally, characteristic switching images are flattened/reshaped to a 1-D vector and fed to the SVM for training and testing.

B. Support-Vector Machine

An SVM is a supervised machine learning model that can be used for regression or binary classification problems [29]. The robust supervised learning machine learning framework provided by an SVM performs effectively in both linear and nonlinear classification problems. A key advantage SVMs have over other supervised machine learning models is their ability to consider both empirical and structural risk minimization, which improves the generalization of their classification capabilities [30]. An SVM was selected as the classification algorithm for this system, due to its linear properties, relatively easy implementation, efficient training and computational complexity, and potential to be extended in future research when considering the effects of additional variables (e.g., dc-link and switching device health).

The datasets used for training or using SVMs are in the form of feature vectors, where each vector is representative of a larger data space. Given a training dataset consisting of M feature vectors (x_i)

$$x = \{x_i\}, 1 \leq i \leq M$$

paired with M output labels (y_i)

$$y = \{y_i\}, 1 \leq i \leq M$$

the SVM's training algorithm generates a classification function which outputs the predicted class label for any unlabeled feature vector input. Feature vectors are first mapped to a higher order dimensional space with dimension equal to the length of the feature vectors. For a linear, binary classification problem, the classification function is then trained to generate a hyperplane,

$f(x)$, in this space that determines the decision boundary for classification. This hyperplane is in the form

$$f(x) = w^T x - b = 0 \quad (4)$$

where w is the M -dimensional normal vector to the hyperplane and b is a scalar [31]. This hyperplane is trained to maximize the distance between itself and the nearest data points from either class, according to the optimization problem

$$\min_{w,b} \frac{1}{M} \sum_{i=1}^M \max\{0, 1 - y_i(w x_i - b)\} + C \|w\|^2 \quad (5)$$

where the binary labels, y_i , for each feature vector, x_i , are either -1 or 1 . C is a misclassification penalty parameter, which is adjusted to control the tradeoff between error frequency and decision rule complexity.

In this research, a multiclass-extended SVM model is used to classify the dc-link capacitor into one of five health classes. The multiclass classification model is based on an error-correcting output code (ECOC) technique [32]. Since standard SVM models can only answer binary classification questions, the ECOC technique formulates a multiclass decision model by first decomposing the multiclass classification problem into several independent binary classification problems, and then combining these results into a holistic result classifier. The SVM ECOC model is implemented with a linear kernel, a one-versus-one coding design, and a box constraint value of 25.

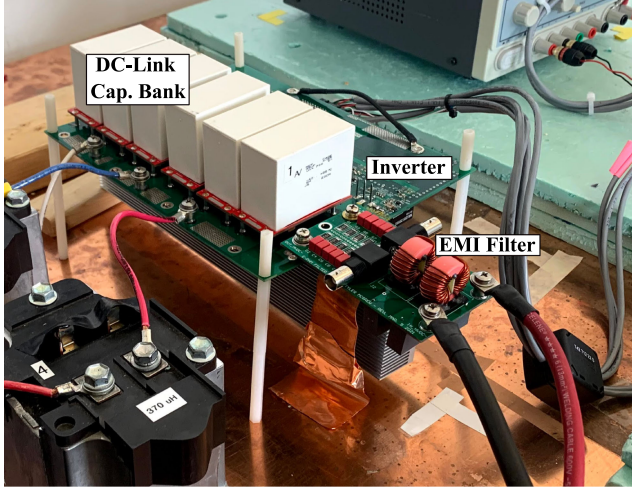
V. EXPERIMENTAL RESULTS

The experimental setup for EMI measurement and EMI filtering are largely the same. Fig. 7 shows the test setup for collecting EMI measurements for the condition monitoring system, which is laid out in Fig. 1, with the addition of a 50- Ω oscilloscope probe placed in parallel with each R_S . HVdc cables coming from the dc power supply and LISNs connect to the proposed EMI filter and measurement board, which is connected in turn to the HVdc inputs of the three-phase inverter. The setup for measuring conducted EMI emissions is the same as the condition monitoring experiment, but an oscilloscope probe with 50- Ω impedance is in parallel with R_{LISN} . This probe connects to the top LISN, while a 50- Ω termination resistor connects to the bottom LISN.

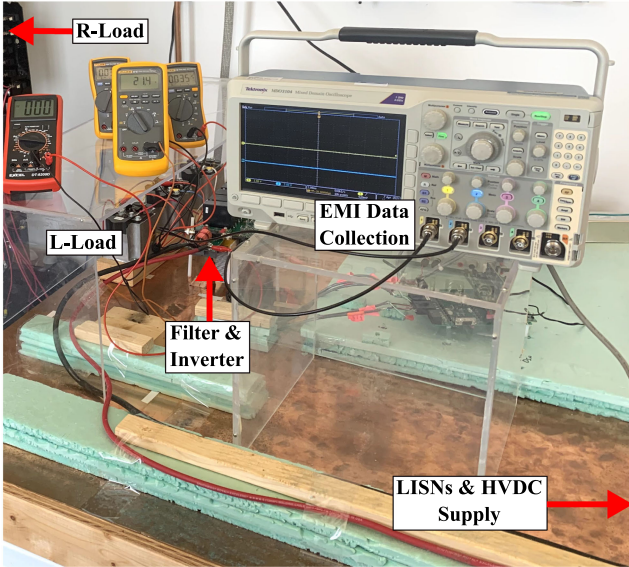
For both conducted emissions testing and EMI measurement collection, the inverter was operated in the same conditions: 270 Vdc, 20-kHz switching frequency, 60-Hz fundamental frequency, and a modulation index of 0.9. The R - L load consists of a 370- μ H inductive component and a 24- Ω resistive component in a Wye configuration.

A. EMI Filtering Results

Conducted emissions testing was evaluated according to the guidelines laid out in CE102 [24]. A summary of EMI filtering results is seen in Fig. 8. In addition to the CE102 conducted emissions measurements, conducted EMI measurements were also collected for differential and CM noise, both with and without the filter. As evidenced in Fig. 8(b), the EMI filter and



(a)



(b)

Fig. 7. Experimental test setup showing (a) inverter, dc-link capacitor bank, and EMI filter/measurement board, and (b) measurement setup with R-L load, multimeters, and oscilloscope.

measurement board successfully reduce the conducted emissions' amplitude below the CE102 standard, with about 10 dB of margin at normal operating conditions. This demonstrates the filtering efficacy of the proposed EMI filter/measurement board.

B. EMI Measurement Results

EMI measurements were collected for each of the five dc-link health classes through the use of two sets of six interchangeable MPPF capacitor boards, representing five stages of capacitor health, from new through aged. These five stages were selected to represent the entire operational lifetime of the dc-link. New capacitor parameters are $C_{DC,N} = 50 \mu\text{F}$, $R_{ESR,N} = 6 \text{ m}\Omega$, and $L_{ESL} = 35 \text{ nH}$, while aged capacitor parameters are $C_{DC,A} = 47.5 \mu\text{F}$, $R_{ESR,A} = 19.4 \text{ m}\Omega$, and $L_{ESL} = 35 \text{ nH}$. The aged capacitor parameters reflect the 10% drop in C_{DC}

TABLE II
DC-LINK CAPACITOR CLASS PARAMETERS

Health Class	Config.	Condition	R_{ESR}	C_{DC}
1	$N^6 A^0$	New	1.000 m Ω	300 μF
2	$N^5 A^1$	Partially Aged	1.130 m Ω	297.5 μF
3	$N^3 A^3$	Half Aged	1.527 m Ω	292.5 μF
4	$N^1 A^5$	Nearly Aged	2.356 m Ω	287.5 μF
5	$N^0 A^6$	Aged	3.323 m Ω	285 μF

and $2\text{--}3\times$ increase in R_{ESR} that are generally regarded as the failure point for film capacitors [8]. By combining new and aged capacitors in parallel, five stages of capacitor health are emulated. These five stages are summarized in Table II.

Condition monitoring data were collected using two oscilloscope probes with 50- Ω measurement impedance. These probes were connected directly to the BNC connections on the board, as seen in Fig. 7. For each of the five classes of dc-link health, two 100-ms samples were collected at 100 MSample/s, for a total of 20 million data points per class on each channel. Using these two sets of data, the conducted differential mode EMI is

$$V_{DM} = \frac{V_{SENSE+} - V_{SENSE-}}{2}.$$

The signal processing and SVM classification steps were implemented in MATLAB for this research. The frequency domain analysis of the experimental EMI data collected from the board is shown in Fig. 9. There are two peaks evident in the frequency analysis shown. The first peak, around 5 MHz, is due to the high-pass effect of the EMI filter board's sensing branch when measured using a 50- Ω oscilloscope probe. The cutoff frequency, f_c , is equal to about 4.4 MHz, from (2). A higher measurement impedance or larger values of C_s could be used to lower this cutoff frequency, if lower frequency EMI content was of interest.

The second peak, around 25 MHz, is the high-frequency EMI ringing generated during switching events which is of interest for this condition monitoring system. There are distinctions between capacitor classes visible throughout this frequency range from 5–50 MHz. These differences are most obvious around 20–30 MHz, especially between the aged ($N^0 A^6$) and nearly aged ($N^1 A^5$) capacitor classes. The peak EMI intensity within this range occurs at about 25 MHz, which supports the EMI mechanism predicted in (3) in Section III. The exact frequency of this high-frequency ringing will vary for a specific inverter based on the L_{ESL} of the dc-link and the C_{OSS} and L_s of the switching devices according to (3).

The experimental data for each class were then converted into the time-frequency domain, as discussed in Section IV. For each capacitor health class, all of the characteristic switching events are averaged in Fig. 10 to visually distinguish changes in the time–frequency EMI profile. From these images, it is evident that the increased damping from the ageing of the dc-link ages reduces the amplitude and duration of ringing in the commutation loop. There may also be a slight increase in peak frequency, but the limited frequency resolution of this method means a small change in frequency is difficult to detect.

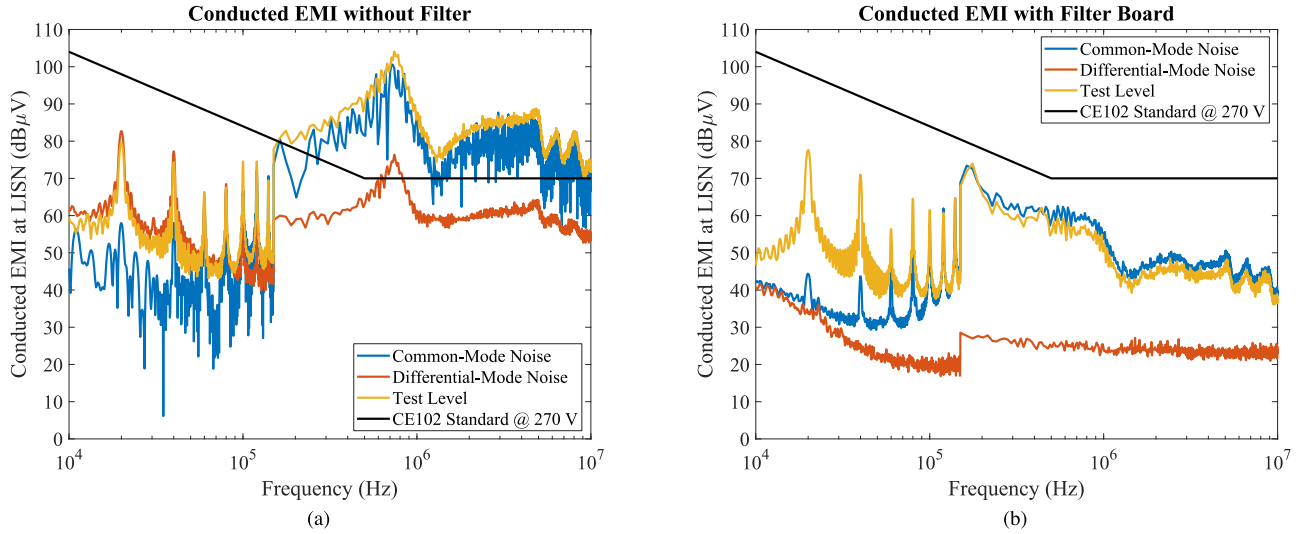


Fig. 8. Summary of differential mode, common mode, and CE102 conducted EMI results (a) without the filter and (b) with the proposed EMI filter and measurement board attached.

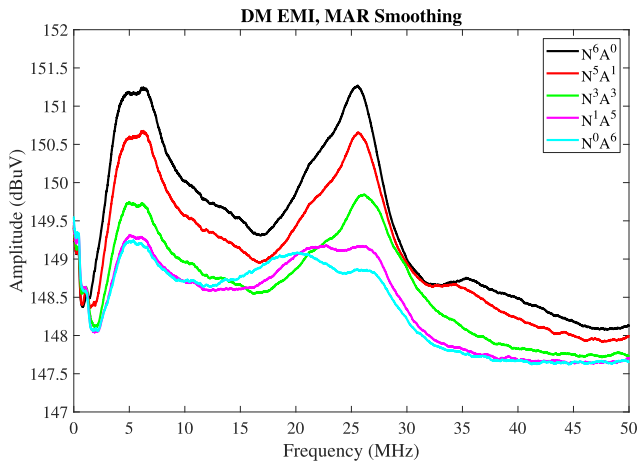


Fig. 9. Frequency analysis of experimental conducted EMI collected for each class of dc-link health, smoothed using a moving average with rectangular window filter (MAR). Apparent peak at 5 MHz is due to the 4.4 MHz cutoff frequency of EMI sensing branch measured with 50- Ω oscilloscope probe, while peak around 25 MHz is the high-frequency ringing of interest.

TABLE III
SVM CLASSIFICATION RESULTS

Number of Averaged T_S	Training Images	Testing Images	Average Accuracy	Maximum Accuracy
1	14000	6000	85.90%	86.32%
5	2800	1200	96.73%	97.25%
10	1400	600	99.19%	99.67%
50	280	120	100.00%	100.00%

C. SVM Classification Results

Once average switching images were created for each T_S , switching events images from multiple T_S were averaged together to supply four different SVM models with training and testing data. The classification results of these models are shown in Table III. Classification accuracy was about 86% for the SVM

model trained using inputs of six averaged switching events (one T_S). However, averaging switching events across more T_S before SVM training/classification results in greater accuracy. This improvement is due to the removal of outliers and noise in the input data. Using only 500 μs of EMI data (10 averaged T_S), this classification system was able to achieve an average accuracy above 99%, demonstrating the effectiveness of this condition monitoring method.

The confusion matrices for each of these four SVM models are shown in Fig. 11. It is evident that the SVM classification models have a relatively harder time differentiating between the two most healthy classes and the two most aged classes, while they are better at discriminating between classes two, three, and four. Additionally, when switching events are averaged for five or more switching periods, the SVM classifications were never more than one class off of the true health class.

D. Practical Implementation

In a real application, the dc-link capacitor will not correspond to the exact parameters of any of the five health classes laid out in this research. However, the linear nature of the multiclass SVM classification system means that the dc-link should be assigned to its nearest health classification. Additionally, if a capacitor was tested which was even more aged than the “aged” class used in this research, it should likely fall in the “aged” class, although this was not confirmed as a part of this research.

The capacitor classes are determined from measurement data taken throughout the lifetime of the capacitor while it is installed in the inverter. These data cannot be obtained for each, individual product produced by a manufacturer. So, the machine-learning algorithm must be trained offline using a handful of production units to implement this method into a commercial product. This will produce an overall profile for the aging process of hardware, not just the capacitor.

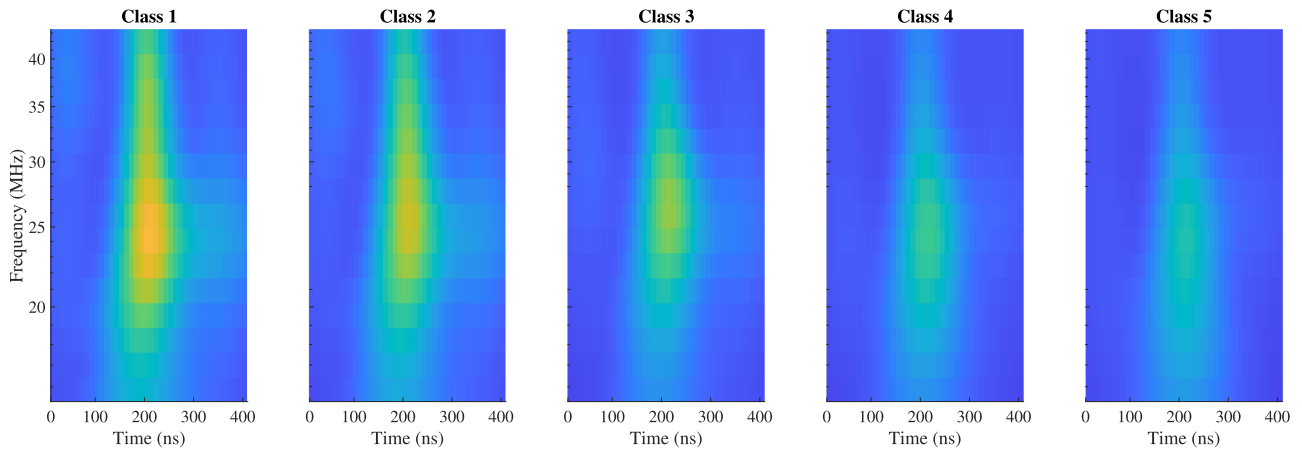


Fig. 10. Switching events averaged across all experimental conducted EMI measurements (4000 T_S) for each class of dc-link capacitor health.

Average Classification Results					
True Class \ Predicted Class	1	2	3	4	5
1	1119	138.8	0	0	0
2	139.3	1048	29.35	0.04	0.9
3	0.03	31.71	1078	34.56	0.57
4	0	0	35.46	936.1	223.9
5	0	0	0	211.3	972.6

(a)

Average Classification Results					
True Class \ Predicted Class	1	2	3	4	5
1	243	5.7	0	0	0
2	5.02	239.3	0.72	0	0
3	0	0	230.3	1.08	0
4	0	0	0.02	229.3	12.09
5	0	0	0	14.62	218.9

(b)

Average Classification Results					
True Class \ Predicted Class	1	2	3	4	5
1	127.1	0.31	0	0	0
2	1.88	125.7	0	0	0
3	0	0	118	0	0
4	0	0	0	113.3	1.01
5	0	0	0	1.68	111

(c)

Average Classification Results					
True Class \ Predicted Class	1	2	3	4	5
1	24	0	0	0	0
2	0	18	0	0	0
3	0	0	27	0	0
4	0	0	0	28	0
5	0	0	0	0	23

(d)

Fig. 11. Confusion matrices of average SVM classification results when switching events images are averaged across (a) 1 T_S , (b) 5 T_S , (c) 10 T_S , and (d) 50 T_S .

Since the capacitor characteristics vary due to manufacturing tolerances, there are differences between the EMI signatures for each unit. To overcome this problem, the training data may be fine-tuned during a burn-in process. Manufacturers perform burn-in testing by running the power electronics at full power for several hours. This eliminates units that fail due to manufacturing defects, or “infant mortality.” Automated test equipment (ATE) controls the products during burn-in, and it typically interfaces with the hardware during the test. Manufacturers can take advantage of this time to offload the performance data from the ATE, fine-tune the algorithms, and flashe the model parameters into hardware’s memory at the end of the burn-in test. This provides a starting point of the hardware, and the algorithm will detect deviations from this starting point. As discussed in Section III, the proposed method is not application-dependent, and should be viable as long as the increase in damping as the dc-link ages is the primary mechanism affecting change in commutation damping, or other causes can be separated out.

VI. CONCLUSION

This article presents a noninvasive condition monitoring system for MPPF dc-link capacitors within three-phase inverters. It is based on time-frequency analysis of conducted EMI. First, an EMI filter and measurement board is introduced, which proves effective in filtering conducted EMI to meet regulatory standards

and sensing high-frequency conducted EMI for condition monitoring use. Then, a novel dc-link health classification system is proposed, which utilizes a CWT to analyze conducted EMI in the time-frequency domain. From these images, switching events are located, averaged, and fed into a SVM classification system which achieves near-perfect average accuracy in experimental conditions. The proposed condition monitoring system provides advantages over other techniques in terms of its low cost, low-invasiveness, online availability, and high accuracy. Both the hardware and software portions of the proposed condition monitoring system present opportunities for future research in terms of other electric components, converter applications, and test conditions.

REFERENCES

- [1] C. Markou and G. Cross, “Airline maintenance cost executive commentary - FY 2019,” Maintenance Cost Task Force, Int. Air Transp. Assoc. (IATA), Montreal, QC, Canada, Jan. 2021.
- [2] U. Periyarselvam, T. Tamilselvan, S. Thilakan, and M. Shanmugaraja, “Analysis on costs for aircraft maintenance,” *Adv. Aerosp. Sci. Appl.*, vol. 3, no. 3, pp. 177–182, 2013.
- [3] R. R. Schoen, T. G. Habetler, F. Kamran, and R. G. Bartheld, “Motor bearing damage detection using stator current monitoring,” *IEEE Trans. Ind. Appl.*, vol. 31, no. 6, pp. 1274–1279, Nov./Dec. 1995.
- [4] A. Soualhi, K. Medjaher, and N. Zerhouni, “Bearing health monitoring based on Hilbert–Huang transform, support vector machine, and regression,” *IEEE Trans. Instrum. Meas.*, vol. 64, no. 1, pp. 52–62, Jan. 2015.

- [5] R. M. Tallam, T. G. Habetler, and R. G. Harley, "Self-commissioning training algorithms for neural networks with applications to electric machine fault diagnostics," *IEEE Trans. Power Electron.*, vol. 17, no. 6, pp. 1089–1095, Nov. 2002.
- [6] D. Xiang, L. Ran, P. Tavner, S. Yang, A. Bryant, and P. Mawby, "Condition monitoring power module solder fatigue using inverter harmonic identification," *IEEE Trans. Power Electron.*, vol. 27, no. 1, pp. 235–247, Jan. 2012.
- [7] R. Biswas and A. Routray, "Application of EMR signature in health assessment and monitoring of IGBT-based converters," *IEEE Trans. Power Electron.*, vol. 35, no. 2, pp. 1899–1906, Feb. 2020.
- [8] H. Wang and F. Blaabjerg, "Reliability of capacitors for DC-link applications in power electronic converters—An overview," *IEEE Trans. Ind. Appl.*, vol. 50, no. 5, pp. 3569–3578, Sep./Oct. 2014.
- [9] Z. Zhao, P. Davari, W. Lu, H. Wang, and F. Blaabjerg, "An overview of condition monitoring techniques for capacitors in DC-link applications," *IEEE Trans. Power Electron.*, vol. 36, no. 4, pp. 3692–3716, Apr. 2021.
- [10] S. Prasanth, M. H. M. Sathik, F. Sasongko, T. C. Seng, M. Tariq, and R. Simanjorang, "Online equivalent series resistance estimation method for condition monitoring of DC-link capacitors," in *Proc. IEEE Energy Convers. Congr. Expo.*, Cincinnati, OH, USA, 2017, pp. 1773–1780.
- [11] P. Sundararajan *et al.*, "Condition monitoring of DC-link capacitors using Goertzel algorithm for failure precursor parameter and temperature estimation," *IEEE Trans. Power Electron.*, vol. 35, no. 6, pp. 6386–6396, Jun. 2020.
- [12] K. Laadjal, M. Sahraoui, A. J. M. Cardoso, and A. M. R. Amaral, "Online estimation of aluminum electrolytic-capacitor parameters using a modified Prony's method," *IEEE Trans. Ind. Appl.*, vol. 54, no. 5, pp. 4764–4774, Sep./Oct. 2018.
- [13] W. Miao, K. H. Lam, and P. W. T. Pong, "Online monitoring of aluminum electrolytic capacitors in photovoltaic systems by magnetoresistive sensors," *IEEE Sensors J.*, vol. 20, no. 2, pp. 767–777, Jan. 2020.
- [14] H. Soliman, P. Davari, H. Wang, and F. Blaabjerg, "Capacitance estimation algorithm based on DC-link voltage harmonics using artificial neural network in three-phase motor drive systems," in *Proc. IEEE Energy Convers. Congr. Expo.*, Cincinnati, OH, USA, 2017, pp. 5795–5802.
- [15] M. W. Ahmad, P. N. Kumar, A. Arya, and S. Anand, "Noninvasive technique for DC-link capacitance estimation in single-phase inverters," *IEEE Trans. Power Electron.*, vol. 33, no. 5, pp. 3693–3696, May 2018.
- [16] W. Lu, X. Lu, J. Han, Z. Zhao, and X. Du, "Online estimation of ESR for DC-link capacitor of boost PFC converter using wavelet transform based time-frequency analysis method," *IEEE Trans. Power Electron.*, vol. 35, no. 8, pp. 7755–7764, Aug. 2020.
- [17] J. E. Timperley and J. M. Vallejo, "Condition assessment of electrical apparatus with EMI diagnostics," *IEEE Trans. Ind. Appl.*, vol. 53, no. 1, pp. 693–699, Jan./Feb. 2017.
- [18] S. Pu, E. Ugur, B. Akin, and H. Akca, "Investigation of EM radiation changes in SiC based converters throughout device aging," in *Proc. IEEE 5th Workshop Wide Bandgap Power Devices Appl.*, 2017, pp. 190–194.
- [19] W. Qiao and L. Qu, "Prognostic condition monitoring for wind turbine drivetrains via generator current analysis," *Chin. J. Elect. Eng.*, vol. 4, no. 3, pp. 80–89, Sep. 2018.
- [20] A. M. Imam, T. G. Habetler, R. G. Harley, and D. Divan, "Failure prediction of electrolytic capacitor using DSP methods," in *Proc. 28th Annu. IEEE Appl. Power Electron. Conf. Expo.*, 2005, vol. 2, pp. 965–970.
- [21] M. Boubin, J. P. Doran, W. Guo, Y. Rajasekhar, and M. Scott, "EMI diagnostics of three phase inverters using machine learning algorithms," in *Proc. IEEE Energy Convers. Congr. Expo.*, Portland, OR, USA, 2018, pp. 4062–4069.
- [22] V. Sysoeva, "Hidden Markov model-supported machine learning for condition monitoring of DC-link capacitors," M.S. thesis, Dept. Elect. Comput. Eng., Miami Univ., Oxford, OH, USA, 2020, Accessed: Mar. 16, 2021. [Online]. Available: http://rave.ohiolink.edu/etdc/view?acc_num=miami1595978044573618
- [23] T. McGrew, V. Sysoeva, C. Cheng, and M. Scott, "Condition monitoring of DC-link capacitors using hidden Markov model supported-convolutional neural network," in *Proc. IEEE Appl. Power Electron. Conf. Expo.*, Phoenix, AZ, USA, 2021, pp. 2323–2330.
- [24] *Requirements for the Control of Electromagnetic Interference Characteristics of Subsystems and Equipment*, MIL-STD-461G, United States Department of Defense, Washington, DC, USA, Mar. 2015.
- [25] M. Gebbia, *Introduction to Film Capacitors*. Des Plaines, IL, USA: Illinois Capacitor, Inc., 2013.
- [26] H. Soliman, H. Wang, and F. Blaabjerg, "A review of the condition monitoring of capacitors in power electronic converters," *IEEE Trans. Ind. Appl.*, vol. 52, no. 6, pp. 4976–4989, Nov./Dec. 2016.
- [27] Y. Gupta, M. W. Ahmad, S. Narale, and S. Anand, "Health estimation of individual capacitors in a bank with reduced sensor requirements," *IEEE Trans. Ind. Electron.*, vol. 66, no. 9, pp. 7250–7259, Sep. 2019.
- [28] J. M. Lilly and S. C. Olhede, "Generalized morse wavelets as a super-family of analytic wavelets," *IEEE Trans. Signal Process.*, vol. 60, no. 11, pp. 6036–6041, Nov. 2012.
- [29] A. Belousov, S. Verzhakov, and J. von Frese, "Applicational aspects of support vector machines," *J. Chemometrics*, vol. 16, no. 8/10, pp. 482–489, Aug. 2002.
- [30] D. Olson and D. Delen, *Advanced Data Mining Techniques*. Berlin, Germany: Springer, 2008.
- [31] A. Widodo and B. Yang, "Support vector machine in machine condition monitoring and fault diagnosis," *Mech. Syst. Signal Process.*, vol. 21, no. 6, pp. 2560–2574, 2007.
- [32] M. Liu, D. Zhang, S. Chen, and H. Xue, "Joint binary classifier learning for ECOC-Based multi-class classification," *IEEE Trans. Pattern Anal. Mach. Intell.*, vol. 38, no. 11, pp. 2335–2341, Nov. 2016.



Tyler McGrew (Student Member, IEEE) received the B.S. degree in electrical engineering from Miami University, Oxford, OH, USA, in 2021. He is currently working toward the M.S. and Ph.D. degrees in electrical engineering with the Center for Power Electronics Systems, Virginia Tech, Blacksburg, VA, USA.

His research interests include modeling and reduction of electromagnetic interference, applications of wide-bandgap power devices, high-frequency power conversion and magnetics, and condition monitoring techniques for power electronics hardware.



Viktoriia Sysoeva received the B.E. degree in nanotechnology from Voronezh State University, Voronezh, Russia, in 2012, the M.S. degree in electronics and nanoelectronics from Voronezh State University, Voronezh, Russia, in 2014, and the M.S. degree in computational electrical and computer engineering from Miami University, Oxford, OH, USA, in 2020.

Her research interests include machine learning, condition monitoring of power electronic systems, and advanced digital signal processing.



Chi-Hao Cheng (Senior Member, IEEE) received the B.S. degree in control engineering from National Chiao Tung University, Hsinchu, Taiwan, in 1991, and the M.S. and Ph.D. degrees in electrical and computer engineering from the University of Texas at Austin, Austin, TX, USA, in 1996 and 1998, respectively.

He is currently a Professor of electrical and computer engineering with Miami University, Oxford, OH, USA. His research interests include digital signal processing, wideband receiver, and optical communications.



Chad Miller received the B.S. degree in computer engineering and the M.S. degree in electrical engineering from Wright State University, Dayton, OH, USA, in 2002 and 2014, respectively.

He is currently an Engineering Program Manager with the Aerospace Systems Directorate, Air Force Research Laboratory, Wright-Patterson Air Force Base, OH, USA. In this capacity, he leads the Intelligent Power Systems research program. He also leads experimental hardware-in-the-loop research and helped develop the advanced power emulator.

His research interests include addressing power stability, power quality, zonal protection, fault tolerance, and emerging technologies through integration, advanced communication, and control.



James Scofield has been a Research Engineer with the Electrical Power Systems Branch of the Aerospace Systems Directorate's Power Division for 34 years. During that time he has been involved in developmental research in the areas of photovoltaics, space power management and distribution systems, high-temperature ohmic contact and packaging metallurgy, power device design and fabrication process development, plasma diagnostics, and semiconductor materials characterization. His current research interests include SiC power technology and multiswitch

power module development capable of providing reliable operation under harsh environmental conditions.



Mark J. Scott (Member, IEEE) received the B.S., M.S., and Ph.D. degrees in electrical engineering from the Ohio State University, Columbus, OH, USA, in 2005, 2013, and 2015, respectively.

His work experience includes developing and installing industrial automation systems and validating power electronics for automotive applications. He is currently an Assistant Professor with Miami University, Oxford, OH, USA. He reviews papers for many conferences and journals. His research interests include the design tradeoffs of using silicon carbide and gallium nitride power devices in electrified transportation, and also prognostic and health management techniques for power conversion hardware.

Dr. Scott was the Local Arrangements Chair for the 2017 IEEE Energy Conversion Congress and Exposition (ECCE), the Publicity Chair for the Workshop on Wide Bandgap Power Devices and Applications in 2018 and 2019, the Financial Chair for ECCE 2018, ECCE 2019, and ECCE 2020, and a Technical Program Committee Member for ECCE 2021.